

Long-Range Spin-Orbit-Coupled Magnetoelectricity in Type-II Multiferroic NiI_2

Weiye Pan,^{1,*} Zefeng Chen,^{2,*} Dezhao Wu,¹ Weiqin Zhu,² Zhiming Xu,¹ Lianchuang Li,² Junsheng Feng,³ Bing-Lin Gu,^{1,4} Wenhui Duan,^{1,4,5,†} and Changsong Xu^{2,6,‡}

¹State Key Laboratory of Low Dimensional Quantum Physics and
Department of Physics, Tsinghua University, Beijing 100084, China

²Key Laboratory of Computational Physical Sciences (Ministry of Education),
Institute of Computational Physical Sciences, State Key Laboratory of Surface Physics,
and Department of Physics, Fudan University, Shanghai 200433, China.

³School of Physics and Materials Engineering, Hefei Normal University, Hefei 230601, China

⁴Institute for Advanced Study, Tsinghua University, Beijing 100084, China

⁵Frontier Science Center for Quantum Information, Beijing 100084, China

⁶Hefei National Laboratory, Hefei 230088, China

Type-II multiferroics, where spin order induces ferroelectricity, exhibit strong magnetoelectric coupling. However, for the typical 2D type-II multiferroic NiI_2 , the underlying magnetoelectric mechanism remains unclear. Here, applying generalized spin-current model, together with first-principles calculations and a tight-binding approach, we build a comprehensive magnetoelectric model for spin-induced polarization. Such model reveals that the spin-orbit coupling extends its influence to the third-nearest neighbors, whose contribution to polarization rivals that of the first-nearest neighbors. By analyzing the orbital-resolved contributions to polarization, our tight-binding model reveals that the long-range magnetoelectric coupling is enabled by the strong e_g - p hopping of NiI_2 . Monte Carlo simulations further predict a Bloch-type magnetic skyrmion lattice at moderate magnetic fields, accompanied by polar vortex arrays. These findings can guide the discovery and design of strongly magnetoelectric multiferroics.

Type-II multiferroicity arises when electric polarization is induced by magnetic order, typically leading to strong magnetoelectric coupling [1–4]. NiI_2 is a typical van der Waals type-II multiferroic that crystallizes in D_{3d} symmetry, featuring triangular-latticed layers of Ni^{2+} ions [Fig. 1(a)]. Each Ni^{2+} ($3d^8$, $S = 1$) carries a local moment of about $2\mu_B$, arranged in a canted screw state propagating along $\langle 1\bar{1}0 \rangle$ directions in the layer [Fig. 1(b, c1)] [5, 6]. A realistic spin model has been developed and demonstrates that the screw originates from competitions of Heisenberg terms and the canting of this screw results from a novel Kitaev interaction [7]. The canted screw induces an in-plane polarization perpendicular to its propagation, giving rise to type-II multiferroicity [6]. Recently, NiI_2 was successfully fabricated in few-layer or monolayer forms, where the helical state shifts to propagate along $\langle 110 \rangle$ directions [8–11], which gives rise to distinct spin rotation plane, as well as possible parallel or perpendicular polarizations [Fig. 1(c2)] [9–11].

Despite the established multiferroic behaviors and the realistic spin model, the magnetoelectric coupling mechanism of NiI_2 remains elusive. From a symmetry perspective, the Ni^{2+} ions occupy inversion centers, thus ruling out both p - d hybridization (where the polarization is induced by the charge transfer between metal and ligand [12–14]) and the anisotropic symmetric exchange mechanism [15]. Moreover, spin-orbit coupling (SOC) has been shown to be essential for generating polarization in NiI_2 [16], which excludes the exchange striction mechanism, since it induces polarization without relying on relativistic effects [17, 18]. In an effort to describe NiI_2 multiferroicity, the KNB (spin-current) model was

applied [19, 20], where the local electric dipole is related to spins via $\mathbf{P}_{\text{KNB}} \propto \mathbf{e}_{ij} \times (\mathbf{S}_i \times \mathbf{S}_j)$, with \mathbf{e}_{ij} being the vector from \mathbf{S}_i to \mathbf{S}_j [21] [Fig. 1(c3)]. Although this model works well for terbium manganite by reproducing the perpendicular polarization arising from its spin cycloid, it fails to predict polarization for a proper screw. In NiI_2 , the KNB scenario is partially satisfied because the canted screw along $\langle 1\bar{1}0 \rangle$ includes a cycloidal component. However, when the proper screw states propagate along $\langle 110 \rangle$ directions, the magnetic point group ($2.1'$) enforces a polarization parallel to the propagation vector [Fig. 1(c4)], and the KNB model fails. Similarly, the KM model, $\mathbf{P}_{\text{KM}} \propto \mathbf{S}_i \times \mathbf{S}_j$ [22], which applies to proper screws, also proves only partially correct for the canted screw state of NiI_2 . Hence, a comprehensive magnetoelectric model, capable of describing all spin-polarization configurations in NiI_2 , is still highly desired.

To obtain an accurate magnetoelectric model for NiI_2 , the generalized spin-current (GSC) method offers a promising avenue [23]. This method incorporates the complete interactions between spins and electric dipole via $\mathbf{P}_{\text{GSC}} = \sum_{\alpha\beta} \mathbf{P}_{ij}^{\alpha\beta} S_{i\alpha} S_{j\beta}$, where the coefficients $\mathbf{P}_{ij}^{\alpha\beta}$ can be determined by fitting to *ab initio* results. Because of its generality, the aforementioned models become special cases of the GSC approach, once the crystal symmetry is taken into account. Indeed, the GSC method has been applied to a range of materials and has successfully described their magnetoelectricity, including CuFeO_2 [14], MnI_2 [23], AgCrO_2 [23], and VI_2 [24, 25], by considering contributions from only the first nearest neighbors (NN). For NiI_2 , the GSC method has also been implemented, again relying on first nearest-neighbor

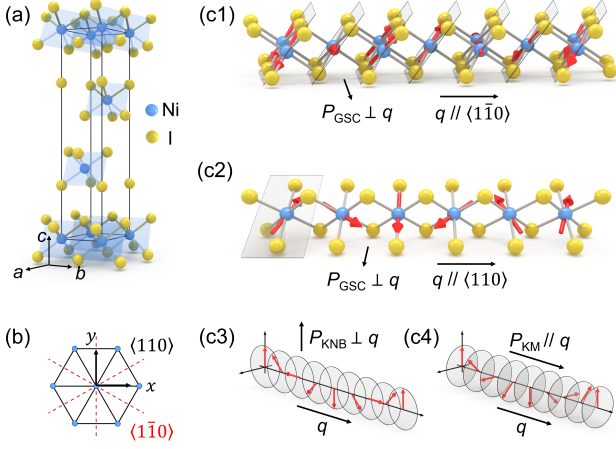


FIG. 1. Schematics of (a) crystal structure of NiI₂ and (b) its top view highlighting key orientations. Panel (c) illustrates four representative noncollinear spin states: (c1) canted screw propagating along $\langle 1\bar{1}0 \rangle$, (c2) canted cycloid propagating along $\langle 110 \rangle$, (c3) a vertical cycloid, and (c4) a proper screw. The half-transparent planes in (c) indicate the spin rotation planes, while the black arrows denote the propagation vector \mathbf{q} and the spin-induced polarization \mathbf{P} .

(1NN) contributions, yet resulting in notable numerical discrepancies [10, 26] (see also our results below). This suggests that further-neighbor interactions may be significant, especially since that the third NN (3NN) exchange J_3 can be comparable to the first NN exchange J_1 . If additional exchange pathways are indeed relevant, questions naturally arise regarding their microscopic origins, how SOC operates over such distances, and whether this can be exploited to engineer stronger magnetoelectricity.

In this Letter, the GSC method, combined with density functional theory (DFT) calculations and a tight-binding (TB) model, is applied to investigate the magnetoelectric behavior of NiI₂ and its electronic origins. Besides the 1NN coupling, the 3NN interaction is found to be even stronger; Including both ensures that the model accurately reproduces the polarization for any spin configurations, not just the magnetic ground state. Interestingly, this phenomenon also appears in NiBr₂ but not in VI₂ or MnI₂. A TB analysis confirms a first-order dependence of polarization on the SOC strength and attributes the enhanced third NN coupling to stronger p - d hopping involving e_g orbitals. Moreover, changes in the spin texture under applied magnetic fields are clarified. Leveraging the present improved model, a complex pattern of polar vortex lattice is predicted.

Magnetoelectric model. We start with applying the GSC method to NiI₂. The presence of inversion centers at the midpoints of 1NN to 3NN enables the simplification

of the GSC model as follows,

$$\mathbf{P}_{\text{GSC}} = \sum_{\langle ij \rangle_n} \mathcal{M}_{ij}^n (\mathbf{S}_i \times \mathbf{S}_j) \quad (1)$$

where \mathcal{M}_{ij}^n is a 3×3 matrix connecting the n th NN of spins \mathbf{S}_i and \mathbf{S}_j . The elements of \mathcal{M} can be determined by the four-state mapping method and DFT calculations [27, 28]. With the D_{3d} symmetry of NiI₂, the relevant \mathcal{M} matrices for pairs along the x -axis (Fig. 1) are found to be (in units of $10^{-5} e\text{\AA}$):

$$\mathcal{M}^1 = \begin{bmatrix} 11 & 0 & 0 \\ 0 & 109 & 139 \\ 0 & -4 & 5 \end{bmatrix}, \quad \mathcal{M}^3 = \begin{bmatrix} -1 & 0 & 0 \\ 0 & 16 & 164 \\ 0 & -12 & -10 \end{bmatrix}.$$

As one can see, the dominant elements include M_{yy}^1 and M_{yz}^1 for the 1NN matrix \mathcal{M}^1 . For instance, a positive M_{yy}^1 implies that, if $\mathbf{S}_i \parallel z$ and $\mathbf{S}_j \parallel x$, then an electric dipole forms along y . Likewise, a positive M_{yz}^1 indicates that $\mathbf{S}_i \parallel x$ and $\mathbf{S}_j \parallel y$ induce a y -directed dipole. Notably, the KNB model corresponds to an antisymmetric matrix with only nonzero entries of $M_{yz}^{\text{KNB}} = -M_{zy}^{\text{KNB}}$, which can be determined as $(M_{yz}^1 - M_{zy}^1)/2 = 72$. Hence, the KNB model actually omits, at least, the major diagonal contribution from M_{yy}^1 . Interestingly, though the \mathcal{M}^2 is found to be negligible, the 3NN matrix \mathcal{M}^3 is significant, featuring the largest element $M_{yz}^3 = 164$ among all the \mathcal{M}^n components. To confirm that M_{yz}^3 indeed exceeds M_{yy}^1 and M_{yz}^1 , tests are performed over a variety of pseudopotentials and Hubbard U values, all of which consistently show $M_{yz}^3 > M_{yy}^1, M_{yz}^1$ [see Table S2 in Supplementary Materials (SM) [28]].

The accuracy of different models is now assessed by examining a screw state propagating along the y direction (one of the $\langle 1\bar{1}0 \rangle$ directions). As the canting angle of spin rotation plane θ evolves from 0° to 90° , the state transforms from a proper screw, through canted screw states, and ultimately approaches an in-plane cycloid. Figure 2(a) shows that the GSC model including $\mathcal{M}^{1,3}$ produces a noticeable x -component of polarization, which is perpendicular to the propagation direction. For the proper screw at $\theta = 0^\circ$, the GSC model predicts $P_x = -145.5 \mu\text{C}/\text{m}^2$. As θ increases from 0° to 90° , P_x reverses sign and continues to increase. In particular, at the characteristic angle $\theta = 35.3^\circ$ determined by the Kitaev interaction, which defines the magnetic ground state of bulk NiI₂ [7], the present GSC model yields $P_x = 424.2 \mu\text{C}/\text{m}^2$. Moreover, the GSC model shows close agreement with DFT for all θ , indicating that the former is highly accurate. In contrast, the KNB model deviates significantly from the DFT results [Fig. 2(a)].

Furthermore, we also investigate a screw state propagating along the x direction (one of the $\langle 110 \rangle$ directions). As shown in Figs. 2(b) and (c), this $\langle 110 \rangle$ -propagated screw state exhibits both parallel and perpendicular polarizations that agree well with DFT. Specifically, the

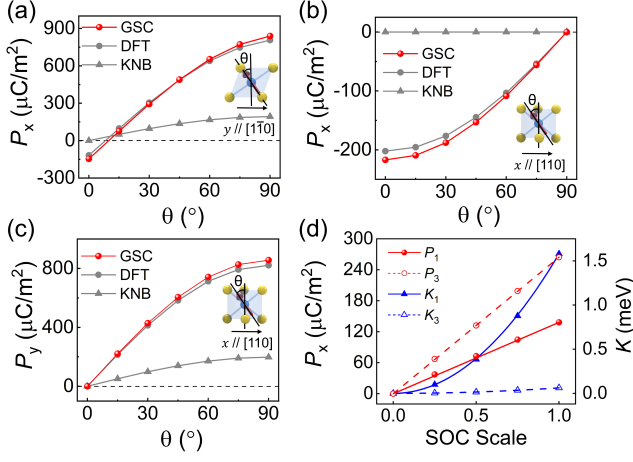


FIG. 2. Spin-induced polarization and its SOC dependence. (a) The x -component of polarization for a screw state propagating along y , plotted against the canting angle θ . (b) and (c) show the x - and y -components of polarization, respectively, for a screw state propagating along x . The P_z component is negligible and thus not shown here. In (a)–(c), data from the GSC model, DFT, and the KNB model are compared; the arrows indicate the propagation directions. (d) The polarization of a canted screw [along y , see Fig. 1(c1)] contributed by 1NN and 3NN spin pairs, as well as 1NN and 3NN Kitaev interactions, as a function of the SOC scale.

parallel component P_x reaches its maximum value of $-217.1 \mu\text{C}/\text{m}^2$ at $\theta = 0^\circ$ and vanishes at $\theta = 90^\circ$, whereas the KNB model predicts zero polarization for all θ . For the perpendicular component P_y , the GSC model yields zero polarization at $\theta = 0^\circ$ and attains a maximum of $856.6 \mu\text{C}/\text{m}^2$ at $\theta = 90^\circ$. In contrast, the KNB model gives much smaller values than DFT does. These findings demonstrate that the induced polarization shifts continuously from being purely parallel to purely perpendicular to the propagation direction. Such transition is accurately captured by the GSC model, but not by either the KNB or KM models. Consequently, the GSC model with contributions from 1NN and 3NN, provides a comprehensive and precise description of the multiferroicity in NiI_2 .

We now examine how polarization depends on SOC by tuning SOC strength in DFT. The $\mathcal{M}^{1,3}$ components are then updated to compute the 1NN and 3NN polarizations. Our calculations adopt the spin state shown in Fig. 1(c1), which propagates along $\langle 1\bar{1}0 \rangle$. Its specific anisotropy arises from the interplay of the Kitaev interaction and single-ion anisotropy [29]. As shown in Fig. 2(d), \mathcal{M}^3 contributes to polarization about 50% more than \mathcal{M}^1 does, further indicating the importance of the 3NN. Both polarization contributions from 1NN and 3NN scale linearly with the SOC strength, indicating that SOC is crucial and extends beyond the nearest neighbors. Interestingly, despite a large J_3/J_1 ratio for the Heisenberg

TABLE I. Dominant \mathcal{M} matrix elements in various compounds. The 1NN and 3NN pairs are both aligned along x direction [see Fig. 1(c2)]. Unit is in $10^{-5} e\text{\AA}$.

	M_{yy}^1	M_{yz}^1	M_{yz}^3		M_{yy}^1	M_{yz}^1	M_{yz}^3
NiI_2	109	139	164	MnI_2	-24	-26	4
NiBr_2	9	16	23	VI_2	-19	13	2

term [7], the 3NN Kitaev interaction, which also arises from SOC, is found to be negligible [Fig. 2(d)].

To understand the long-range impact of SOC, we investigate similar compounds, including NiBr_2 [26], VI_2 [24], and MnI_2 [23], which all exhibit polarization induced by noncollinear spin textures. The dominant \mathcal{M} elements are summarized in Table I. It shows that NiBr_2 , possessing the same $3d^8$ occupation as NiI_2 , also exhibits $M_{yz}^3 > M_{yy}^1, M_{yz}^1$, though these values are about an order smaller than those of NiI_2 due to weaker SOC of Br. In contrast, for MnI_2 ($3d^5$ high spin) and VI_2 ($3d^3$ high spin), M_{yy}^1 and M_{yz}^1 are already small, and M_{yz}^3 is even smaller of an order. These findings suggest that d -orbital occupation plays a key role in producing the large SOC-induced \mathcal{M}^3 contribution.

Tight-binding interpretation. To clarify the electronic origins of the large \mathcal{M}^3 , we construct a tight-binding (TB) model. As shown in Fig. 3(a), a cluster containing three Ni ions and four ligand I anions are considered. The Ni- d and I- p orbitals are included, which appear near the Fermi level as determined by DFT calculations. We adopt a similar approach as in Refs. [21, 23], and express the Hamiltonian $\hat{\mathcal{H}}$ in three parts,

$$\hat{\mathcal{H}} = \hat{H}_{\text{Ni}} + \hat{H}_{\text{I}} + \hat{H}_t \quad (2)$$

where the first part can be further expanded as $\hat{H}_{\text{Ni}} = \hat{H}_{\text{Ni}}^{\text{on}} + \hat{H}_{\text{Ni}}^{\text{SOC}} + \hat{H}_{\text{Ni}}^U$, which are onsite, SOC and Hubbard U terms of Ni, respectively. The second part can similarly expanded as $\hat{H}_{\text{I}} = \hat{H}_{\text{I}}^{\text{on}} + \hat{H}_{\text{I}}^{\text{SOC}}$ for ligand I. The third part represents the hopping process,

$$\hat{H}_t = \sum_{i=1}^3 \sum_{j=1}^4 \sum_{\alpha\beta} \sum_{\sigma=\uparrow,\downarrow} \left(t_{i\alpha j\beta} \hat{p}_{\beta\sigma}^\dagger \hat{d}_{a\alpha\sigma} + \text{h.c.}, \right) \quad (3)$$

where the sums over i, j run over Ni and I, respectively, while the indices (α, β) and σ represent orbital and spin. The hopping term $t_{i\alpha j\beta}$ is constructed with the Slater-Koster integrals $t_{pd\sigma}$ and $t_{pd\pi}$, see Fig. 3(b) and Table III in End Matter. Note that details of such TB model can be found in End Matter.

For each spin configuration K , we diagonalize \mathcal{H} to obtain the ground state $|G_K\rangle$. Summing $\langle G_K | e\vec{r} | G_K \rangle$ over all electrons yields the electronic dipole, from which the $\mathcal{M}_{\text{TB}}^n$ coefficients are determined via the four-state mapping method. Within this TB framework, the ratio $\mu = M_{y'z'}^3 / M_{y'z'}^1$ is found to be 1.09, while $\nu = K_3 / K_1$

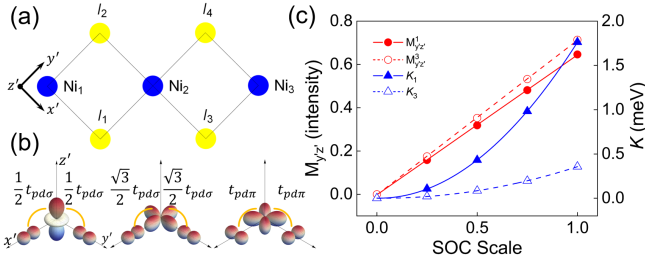


FIG. 3. The setups and results of TB model. Panel (a) schematizes the cluster used in the TB model, containing three Ni ions and four ligand I anions. (b) Three types of hoppings used in the model. (c) Variation of $M_{y'z'}$, as well as Kitaev interaction, for 1NN and 3NN as a function of SOC scale. Note that only e_g orbitals are considered for NiI_2 in the hole representation.

is merely 0.20. In addition, the linear dependence of M and the quadratic dependence of Kitaev interaction K on spin-orbit coupling are both well reproduced [Fig. 3(c)], in excellent agreement with DFT. Furthermore, the ratios μ and ν are found robust against variations in SOC scale λ , charge-transfer energy Δ_{pd} , crystal field Δ_{cf} , hopping integrals and Hubbard U [Fig. 5].

To gain a deeper understanding, we examine the orbital-resolved contributions to the M parameters. In our model, NiI_2 is treated in the hole representation for the high-spin d^8 state, effectively placing two holes in the e_g orbitals. As shown in Table II, the dominant contributions to $\langle \hat{d}_\alpha | e\vec{r} | \hat{p}_\beta \rangle$ indeed originate from these e_g orbitals and remain significant up to 3NN. By contrast, in a system with three electrons (or holes) in the t_{2g} orbitals (as in VI_2), $M_{y'z'}$ is already small at 1NN and becomes negligible at 3NN, indicating a much weaker long-range effect. These differences arise from the edge-sharing octahedral geometry, where e_g - p hopping is substantially larger than the t_{2g} - p hopping ($t_{pd\sigma} > t_{pd\pi}$). As a result, NiI_2 benefits from stronger long-range SOC effects, giving rise to a sizable $M_{y'z'}^3$. Conversely, the Kitaev

TABLE II. Orbital-resolved contributions to the dominant $M_{y'z'}$ elements. This table shows the intensities of each component $\langle \hat{d}_\alpha | e\vec{r} | \hat{p}_\beta \rangle$ in the TB coordinates $\{x', y', z'\}$ for 1NN and 3NN spin pairs. Here e is the elementary charge and \vec{r} is the corresponding position. The t_{2g} orbitals correspond to the case of VI_2 , and the e_g orbitals to the hole representation of NiI_2 .

$M_{y'z'}$	1NN		3NN	
$\sum_\beta \langle \hat{d}_{x'^2-y'^2} e\vec{r} \hat{p}_\beta \rangle$	-1.09	0.65	0.30	0.71
$\sum_\beta \langle \hat{d}_{z'^2} e\vec{r} \hat{p}_\beta \rangle$	1.74		0.41	
$\sum_\beta \langle \hat{d}_{x'y'} e\vec{r} \hat{p}_\beta \rangle$	0.61		-0.13	
$\sum_\beta \langle \hat{d}_{y'z'} e\vec{r} \hat{p}_\beta \rangle$	-0.01	0.60	0.00	-0.12
$\sum_\beta \langle \hat{d}_{z'x'} e\vec{r} \hat{p}_\beta \rangle$	0.00		0.01	

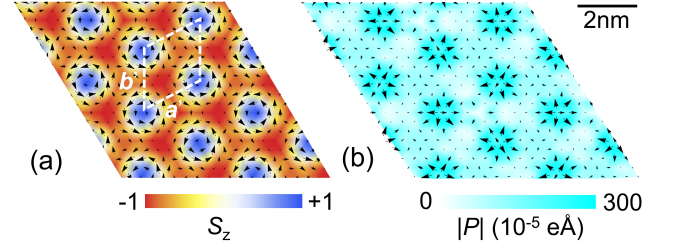


FIG. 4. Magnetic skyrmion lattice and polar vortex pattern in monolayer NiI_2 . Panel (a) the Bloch-type skyrmion lattice under a 30 T field, where the black arrows denote in-plane spins and the warm-cold color map depicts the out-of-plane spin component. The vectors \mathbf{a}' and \mathbf{b}' mark the skyrmion lattice unit cell. (b) The corresponding spin-induced polar vortex pattern, with black arrows showing the in-plane polarization and the color scale indicating the overall polarization magnitude (which is predominantly in-plane).

interaction, which is more sensitive to the t_{2g} - p hopping ($pd\pi$), quickly diminishes over distance. Moreover, Table II suggests that CoI_2 , possessing a high-spin d^7 configuration, may exhibit robust and even stronger M values for both 1NN and 3NN.

Polar vortex lattice. Lastly, we apply the GSC model to explore polar textures in monolayer NiI_2 . Starting from the monolayer ground state, $\langle 110 \rangle$ -propagating canted cycloid [Fig. 1(c2)], we apply an out-of-plane magnetic field B in Monte Carlo simulations (see SM for the spin Hamiltonian [28]). For $B \approx 30$ T, a Bloch-type skyrmion lattice emerges [Fig. 4(a)], where each skyrmion carries topological charge 1 and the lattice constant is about 5.8 times of the crystal lattice constant [30]. Applying the GSC model in Eq. 1 to this spin texture predicts polar vortex pattern [Fig. 4(b)]. The polarization lies mostly in-plane, pointing radially outward from each skyrmion core, with the maximum polarization occurring at the core. It decays significantly beyond the skyrmion region. These polar vortices form a triangular lattice mirroring the underlying skyrmion arrangement. Interestingly, if the chirality of the initial screw state switches (the induced polarization flips), the outward-pointing polar vortices become inward-pointing ones.

In summary, the magnetoelectric mechanism in type-II multiferroic NiI_2 is investigated by developing a first-principles-based GSC model. It is found that third-nearest-neighbor spin pairs contribute a polarization comparable to that of first-nearest neighbors, rooting in the stronger $pd\sigma$ hopping involving e_g orbitals of Ni^{2+} . By including both 1NN and 3NN spin pairs, the model accurately reproduces polarization for a variety of spin patterns and captures diverse polarization textures, including a polar vortex lattice under moderate fields. These findings clarify the mechanism behind spin-induced polarization in NiI_2 and reveal new opportunities

for exploring rich multiferroic phases in layered magnets.

The work at Fudan is supported by NSFC (Grant No. 12274082), National Key R&D Program of China (Grant No. 2022YFA1402901), Shanghai Pilot Program for Basic Research-FuDan University 21TQ1400100 (Grant No. 23TQ017), Shanghai Science and Technology Committee (Grant No. 23ZR1406600), Innovation Program for Quantum Science and Technology (Grant No. 2024ZD0300102), and Xiaomi Young Talents Program. W.D. acknowledges the Basic Science Center Project of NSFC (grant no. 52388201), Innovation Program for Quantum Science and Technology (2023ZD0300500), the Beijing Advanced Innovation Center for Future Chip (ICFC), and the Beijing Advanced Innovation Center for Materials Genome Engineering. J.F. acknowledges the Scientific Research Project of Universities in Anhui Province - 2024AH040216.

* Contributed equally to this work.

† duanw@tsinghua.edu.cn

‡ csxu@fudan.edu.cn

- [1] M. Fiebig, T. Lottermoser, D. Meier, and M. Trassin, The evolution of multiferroics, *Nat. Rev. Mater.* **1**, 1 (2016).
- [2] N. A. Spaldin and R. Ramesh, Advances in magnetoelectric multiferroics, *Nat. Mater.* **18**, 203 (2019).
- [3] S.-W. Cheong and M. Mostovoy, Multiferroics: a magnetic twist for ferroelectricity, *Nat. Mater.* **6**, 13 (2007).
- [4] C. Xu, H. Yu, J. Wang, and H. Xiang, First-principles approaches to magnetoelectric multiferroics, *Annu. Rev. Condens. Matter Phys.* **15**, 85 (2024).
- [5] S. Kuindersma, J. Sanchez, and C. Haas, Magnetic and structural investigations on NiI_2 and CoI_2 , *Physica B+C* **111**, 231 (1981).
- [6] T. Kurumaji, S. Seki, S. Ishiwata, H. Murakawa, Y. Kaneko, and Y. Tokura, Magnetoelectric responses induced by domain rearrangement and spin structural change in triangular-lattice helimagnets NiI_2 and CoI_2 , *Phys. Rev. B* **87**, 014429 (2013).
- [7] X. Li, C. Xu, B. Liu, X. Li, L. Bellaiche, and H. Xiang, Realistic spin model for multiferroic NiI_2 , *Phys. Rev. Lett.* **131**, 036701 (2023).
- [8] M.-P. Miao, N. Liu, W.-H. Zhang, D.-B. Wang, W. Ji, and Y.-S. Fu, Spin-resolved imaging of atomic-scale helimagnetism in monolayer NiI_2 , *arXiv:2309.16526* (2023).
- [9] M. Amini, A. O. Fumega, H. González-Herrero, V. Vaño, S. Kezilebieke, J. L. Lado, and P. Liljeroth, Atomic-scale visualization of multiferroicity in monolayer NiI_2 , *Adv. Mater.* **36**, 2311342 (2024).
- [10] Q. Song, C. A. Occhialini, E. Ergeçen, B. Ilyas, D. Amoroso, P. Barone, J. Kapeghian, K. Watanabe, T. Taniguchi, A. S. Botana, *et al.*, Evidence for a single-layer van der waals multiferroic, *Nature* **602**, 601 (2022).
- [11] H. Ju, Y. Lee, K.-T. Kim, I. H. Choi, C. J. Roh, S. Son, P. Park, J. H. Kim, T. S. Jung, J. H. Kim, *et al.*, Possible persistence of multiferroic order down to bilayer limit of van der waals material NiI_2 , *Nano Lett.* **21**, 5126 (2021).
- [12] T.-h. Arima, Ferroelectricity induced by proper-screw type magnetic order, *J. Phys. Soc. Jpn.* **76**, 073702 (2007).
- [13] C. Jia, S. Onoda, N. Nagaosa, and J. H. Han, Bond electronic polarization induced by spin, *Phys. Rev. B* **74**, 224444 (2006).
- [14] W. Zhu, P. Wang, H. Zhu, H. Zhu, X. Li, J. Zhao, C. Xu, and H. Xiang, Mechanism of type-II multiferroicity in pure and Al-doped CuFeO_2 , *Phys. Rev. Lett.* **134**, 066801 (2025).
- [15] J. Feng and H. Xiang, Anisotropic symmetric exchange as a new mechanism for multiferroicity, *Phys. Rev. B* **93**, 174416 (2016).
- [16] A. O. Fumega and J. Lado, Microscopic origin of multiferroic order in monolayer NiI_2 , *2D Mater.* **9**, 025010 (2022).
- [17] I. A. Sergienko, C. Şen, and E. Dagotto, Ferroelectricity in the magnetic E-phase of orthorhombic perovskites, *Phys. Rev. Lett.* **97**, 227204 (2006).
- [18] S. Picozzi, K. Yamauchi, B. Sanyal, I. A. Sergienko, and E. Dagotto, Dual nature of improper ferroelectricity in a magnetoelectric multiferroic, *Phys. Rev. Lett.* **99**, 227201 (2007).
- [19] Y. Wu, Z. Zeng, H. Lu, X. Han, C. Yang, N. Liu, X. Zhao, L. Qiao, W. Ji, R. Che, *et al.*, Coexistence of ferroelectricity and antiferroelectricity in 2D van der waals multiferroic, *Nat. Commun.* **15**, 8616 (2024).
- [20] T. V. Antão, J. L. Lado, and A. O. Fumega, Electric field control of moiré skyrmion phases in twisted multiferroic NiI_2 bilayers, *Nano Lett.* **24**, 15767 (2024).
- [21] H. Katsura, N. Nagaosa, and A. V. Balatsky, Spin current and magnetoelectric effect in noncollinear magnets, *Phys. Rev. Lett.* **95**, 057205 (2005).
- [22] Q. Zhang, K. Singh, F. Guillou, C. Simon, Y. Breard, V. Caignaert, and V. Hardy, Ordering process and ferroelectricity in a spinel derived from FeV_2O_4 , *Phys. Rev. B* **85**, 054405 (2012).
- [23] H. J. Xiang, E. J. Kan, Y. Zhang, M.-H. Whangbo, and X. G. Gong, General theory for the ferroelectric polarization induced by spin-spiral order, *Phys. Rev. Lett.* **107**, 157202 (2011).
- [24] C. Liu, W. Ren, and S. Picozzi, Spin-chirality-driven multiferroicity in van der waals monolayers, *Phys. Rev. Lett.* **132**, 086802 (2024).
- [25] S. Yu, Y. Xu, Y. Dai, D. Sun, B. Huang, and W. Wei, Interlayer magnetoelectric coupling in van der waals structures, *Phys. Rev. B* **109**, L100402 (2024).
- [26] H.-S. Yu, X.-S. Ni, D.-X. Yao, and K. Cao, Microscopic origin of magnetoferroelectricity in monolayer NiBr_2 and NiI_2 , *arXiv:2501.05025* (2025).
- [27] H. Xiang, P. Wang, M.-H. Whangbo, and X. Gong, Unified model of ferroelectricity induced by spin order, *Phys. Rev. B* **88**, 054404 (2013).
- [28] See Supplementary Materials for more details about calculation methods and further discussions, which includes Refs.[4, 7, 8, 23, 24, 26, 29, 31–44].
- [29] L. Li, B. Zhang, Z. Chen, C. Xu, and H. Xiang, Effects of ktaev interaction on magnetic order and anisotropy, *Phys. Rev. B* **110**, 214435 (2024).
- [30] Such state is reminiscent of that in Ref. [44], where bi-quadratic interaction is neglected and skyrmions exhibit topological charge 2.
- [31] G. Kresse and J. Furthmüller, Efficient iterative schemes for ab initio total-energy calculations using a plane-wave basis set, *Phys. Rev. B* **54**, 11169 (1996).
- [32] J. P. Perdew, K. Burke, and M. Ernzerhof, Generalized

gradient approximation made simple, *Phys. Rev. Lett.* **77**, 3865 (1996).

- [33] N. Liu, C. Wang, C. Yan, C. Xu, J. Hu, Y. Zhang, and W. Ji, Competing multiferroic phases in monolayer and few-layer NiI_2 , *Phys. Rev. B* **109**, 195422 (2024).
- [34] A. S. Botana and M. R. Norman, Electronic structure and magnetism of transition metal dihalides: Bulk to monolayer, *Phys. Rev. Mater.* **3**, 044001 (2019).
- [35] S. Grimme, J. Antony, S. Ehrlich, and H. Krieg, A consistent and accurate ab initio parametrization of density functional dispersion correction (DFT-D) for the 94 elements H-Pu, *J. Chem. Phys.* **132**, 154104 (2010).
- [36] R. D. King-Smith and D. Vanderbilt, Theory of polarization of crystalline solids, *Phys. Rev. B* **47**, 1651 (1993).
- [37] F. Lou, X. Li, J. Ji, H. Yu, J. Feng, X. Gong, and H. Xiang, PASP: Property analysis and simulation package for materials, *J. Chem. Phys.* **154**, 114103 (2021).
- [38] W. Pan, C. Xu, X. Li, Z. Xu, B. Liu, B.-L. Gu, and W. Duan, Chiral magnetism in lithium-decorated monolayer CrTe_2 : Interplay between dzyaloshinskii-moriya interaction and higher-order interactions, *Phys. Rev. B*

109, 214405 (2024).

- [39] C. Xu, X. Li, P. Chen, Y. Zhang, H. Xiang, and L. Bellaiche, Assembling diverse skyrmionic phases in Fe_3GeTe_2 monolayers, *Adv. Mater.* **34**, 2107779 (2022).
- [40] J. Y. Ni, X. Y. Li, D. Amoroso, X. He, J. S. Feng, E. J. Kan, S. Picozzi, and H. J. Xiang, Giant biquadratic exchange in 2D magnets and its role in stabilizing ferromagnetism of NiCl_2 monolayers, *Phys. Rev. Lett.* **127**, 247204 (2021).
- [41] X.-Y. Li, F. Lou, X.-G. Gong, and H. Xiang, Constructing realistic effective spin hamiltonians with machine learning approaches, *New J. Phys.* **22**, 053036 (2020).
- [42] K. Hukushima and K. Nemoto, Exchange monte carlo method and application to spin glass simulations, *J. Phys. Soc. Jpn* **65**, 1604 (1996).
- [43] E. Stiefel, Methods of conjugate gradients for solving linear systems, *J. Res. Nat. Bur. Standards* **49**, 409 (1952).
- [44] D. Amoroso, P. Barone, and S. Picozzi, Spontaneous skyrmionic lattice from anisotropic symmetric exchange in a Ni-halide monolayer, *Nat. Commun.* **11**, 5784 (2020).

End Matter

Setups of TB model. The TB Hamiltonian is constructed as,

$$\hat{\mathcal{H}} = \hat{H}_{\text{Ni}} + \hat{H}_{\text{I}} + \hat{H}_t.$$

The first term $\hat{H}_{\text{Ni}} = \hat{H}_{\text{Ni}}^{\text{on}} + \hat{H}_{\text{Ni}}^{\text{SOC}} + \hat{H}_{\text{Ni}}^U$, is used to describe Ni^{2+} , where $\hat{H}_{\text{Ni}}^{\text{on}}$ is on-site energy term of d orbitals:

$$\hat{H}_{\text{Ni}}^{\text{on}} = \sum_{i=1}^3 \sum_{\sigma=\uparrow,\downarrow} \left[\sum_{\alpha \in t_{2g}} E_{t_{2g}} \hat{d}_{i\alpha\sigma}^\dagger \hat{d}_{i\alpha\sigma} + \sum_{\alpha \in e_g} E_{e_g} \hat{d}_{i\alpha\sigma}^\dagger \hat{d}_{i\alpha\sigma} \right],$$

$\hat{H}_{\text{Ni}}^{\text{SOC}}$ is the SOC effect of magnetic ions:

$$\hat{H}_{\text{Ni}}^{\text{SOC}} = \lambda_{\text{Ni}} \sum_{i=1}^3 (\mathbf{L}_i \cdot \mathbf{S}_i),$$

and \hat{H}_{Ni}^U denotes the effective Zeeman energy, which originates from the local Coulomb repulsion and Hund coupling in the magnetically ordered phase:

$$\hat{H}_{\text{Ni}}^U = -U \sum_{i=1}^3 \sum_{\alpha \in t_{2g}, e_g} \mathbf{m}_i \cdot \mathbf{S}_{i\alpha}.$$

Similarly, the second term $\hat{H}_{\text{I}} = \hat{H}_{\text{I}}^{\text{on}} + \hat{H}_{\text{I}}^{\text{SOC}}$, is used to describe ligand I^- , where $\hat{H}_{\text{I}}^{\text{on}}$ is on-site energy terms of p orbitals:

$$\hat{H}_{\text{I}}^{\text{on}} = E_p \sum_{j=1}^4 \sum_{\beta \in x, y, z} \sum_{\sigma=\uparrow,\downarrow} \hat{p}_{j\beta\sigma}^\dagger \hat{p}_{j\beta\sigma},$$

$\hat{H}_{\text{I}}^{\text{SOC}}$ is the SOC effect of ligand anions:

$$\hat{H}_{\text{I}}^{\text{SOC}} = \lambda_{\text{I}} \sum_{j=1}^4 (\mathbf{L}_j \cdot \mathbf{S}_j).$$

The hopping term \hat{H}_t is introduced in the main text and the hopping integrals are shown in Table III.

TABLE III. Hopping integrals between magnetic ions and ligands in edge-sharing octahedra. The left side shows the case where the Ni-I bond is oriented along the x' -axis, while the right side illustrates the bond along the y' -axis.

	along \hat{x}	p_x	p_y	p_z	along \hat{y}	p_x	p_y	p_z
t_{2g}	d_{xy}	0	$t_{pd\pi}$	0	d_{xy}	$t_{pd\pi}$	0	0
	d_{yz}	0	0	0	d_{yz}	0	0	$t_{pd\pi}$
	d_{zx}	0	0	$t_{pd\pi}$	d_{zx}	0	0	0
e_g	$d_{x^2-y^2}$	$\frac{\sqrt{3}t_{pd\sigma}}{2}$	0	0	$d_{x^2-y^2}$	0	$\frac{\sqrt{3}t_{pd\sigma}}{2}$	0
	d_{z^2}	$-\frac{t_{pd\sigma}}{2}$	0	0	d_{z^2}	0	$-\frac{t_{pd\sigma}}{2}$	0

The following parameters are adopted for the TB simulations. The orbital energies $E_{t_{2g}} = 0$ eV, $E_{e_g} = 1$ eV, $E_p = -2$ eV are estimated from the DFT band structure. To facilitate the calculation, we switch to the hole representation: $E_{t_{2g}} = 1$ eV, $E_{e_g} = 0$ eV, $E_p = 2$ eV. The SOC coefficient $\lambda_{\text{Ni}} = -0.02$ eV and $\lambda_{\text{I}} = -0.27$ eV is extracted from DFT calculations. The Hund term $U = 3$ eV, the hopping integrals $t_{pd\sigma} = 1.6$ eV and $t_{pd\pi} = 0.6$ eV are commonly used values [15, 23]. The dependence of results on such parameters is shown in Fig. 5.

Methods to obtain \mathcal{M} . As aforementioned in the introduction, the local electric dipole in GSC model can be calculated with

$$\mathbf{P}_{ij}^{\text{GSC}} = \sum_{\alpha\beta} \mathbf{P}_{ij}^{\alpha\beta} S_{i\alpha} S_{j\beta}.$$

Applying spatial inversion symmetry and time-reversal symmetry [23], it can be simplified as,

$$\mathbf{P}_{ij}^{\text{GSC}} = \mathcal{M}_{ij} (\mathbf{S}_i \times \mathbf{S}_j),$$

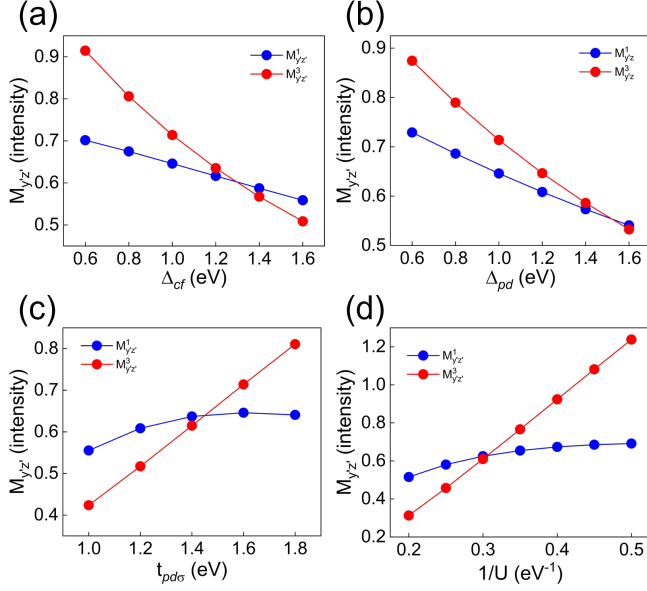


FIG. 5. Dependence of the $M^1_{y'z'}$ and $M^3_{y'z'}$ on tight binding parameters: (a) charge transfer energy Δ_{pd} , (b) crystal field splitting Δ_{CF} , (c) hopping integral $t_{pd\sigma}$ and (d) Hubbard U term.

with

$$\mathcal{M} = \begin{pmatrix} (Pyz)_x & (Pzx)_x & (Pxy)_x \\ (Pyz)_y & (Pzx)_y & (Pxy)_y \\ (Pyz)_z & (Pzx)_z & (Pxy)_z \end{pmatrix}.$$

where the subscripts ij for \mathcal{M} and P are omitted for simplicity.

We employ the four-state mapping method to obtain the \mathbf{P}_{GSC} and \mathcal{M} coefficients. For instance, to extract

$M_{y'z'} = (P^{x'y'})_{y'}$, we compute the ground states ($|G_I\rangle$, $|G_{II}\rangle$, $|G_{III}\rangle$, and $|G_{IV}\rangle$) for four magnetic configurations:

- (I). S_1 along $+x'$ and S_3 along $+y'$;
- (II). S_1 along $+x'$ and S_3 along $-y'$;
- (III). S_1 along $-x'$ and S_3 along $+y'$;
- (IV). S_1 along $-x'$ and S_3 along $-y'$.

Here, S_2 is always aligned along $+z'$ being perpendicular to S_1 and S_3 , with $S = 1$. The $M_{y'z'}$ can then be extracted with

$$M_{y'z'} = \frac{e}{4S^2} \left(\sum_I \langle G_I | \hat{y} | G_I \rangle - \sum_{II} \langle G_{II} | \hat{y} | G_{II} \rangle - \sum_{III} \langle G_{III} | \hat{y} | G_{III} \rangle + \sum_{IV} \langle G_{IV} | \hat{y} | G_{IV} \rangle \right),$$

where the sums run over degenerate ground state(s). The adopted cluster shown in Fig. 3(a) exhibits D_{2h} symmetry, which requires the \mathcal{M}_{TB} matrix in the form of

$$\mathcal{M}_{TB} = \begin{bmatrix} 0 & 0 & -M_{y'z'} \\ 0 & 0 & M_{y'z'} \\ -M_{z'y'} & M_{z'y'} & 0 \end{bmatrix}.$$

The $\mathcal{M}^{1,3}$ matrices are determined as follows:

$$\mathcal{M}_{TB}^1 = \begin{bmatrix} 0 & 0 & -0.65 \\ 0 & 0 & 0.65 \\ 0.00 & -0.00 & 0 \end{bmatrix},$$

$$\mathcal{M}_{TB}^3 = \begin{bmatrix} 0 & 0 & -0.71 \\ 0 & 0 & 0.71 \\ 0.02 & -0.02 & 0 \end{bmatrix}.$$

Note that (i) only the relative values are physically meaningful and (ii) the use of other reasonable parameters will not qualitatively change the results that $M^3_{y'z'}$ is comparable to $M^1_{y'z'}$, as shown in Fig. 5.